Tribol Lett (2007) 28:263–274
DOI 10.1007/s11249-007-9270-5

ORIGINAL PAPER

In Situ Analysis of Third Body Contributions to Sliding Friction of a Pb–Mo–S Coating in Dry and Humid Air

S. D. Dvorak · K. J. Wahl · I. L. Singer

Received: 30 May 2007 / Accepted: 6 September 2007 / Published online: 29 September 2007

Abstract Reciprocating sliding tests of ion-beam deposited (IBD) Pb–Mo–S coatings were performed with an in situ tribometer that allows real-time visualization and Raman analysis of the sliding contact through a transparent hemisphere. Experiments were performed in dry air, ambient air (~50% RH) and mixtures of dry and humid air cycled between low and high humidity. Third bodies formed in the sliding contact were monitored through an optical microscope and analyzed by Raman Spectroscopy. Third body velocity accommodation modes were identified and correlated with friction behavior in dry and ambient air. The dominant velocity accommodation mode in both dry and humid air was interfacial sliding between the outer surface of the transfer film and the wear track; this interface, based on present and earlier studies, is crystalline MoS_2. Therefore, the friction coefficient was controlled by the interfacial shear strength of MoS_2 sliding against MoS_2. Humid air sliding was accompanied by a rise in the friction coefficient and a small but observable second velocity accommodation mode: shear/extrusion of the transfer film. It is concluded that the friction rise in humid air was due to an increase in the interfacial shear strength, and that the rise in friction caused the third body to deform rather than the deformation causing the friction to rise.

Keywords MoS_2 · Solid lubrication · In situ tribology · Velocity accommodation · Rheology

S. D. Dvorak
University of Maine, Orono, ME 04469-5711, USA

K. J. Wahl (✉) · I. L. Singer
Tribology Section, Code 6176, U.S. Naval Research Laboratory, 4555 Overlook Ave. SW, Washington, DC 20375-5342, USA
e-mail: kathryn.wahl@nrl.navy.mil

1 Introduction

MoS_2 coatings have outstanding tribological properties—low friction coefficients and long life—in vacuum or dry gas environments [1, 2]. However, the tribological properties of MoS_2 are degraded severely when humidity is present [3, 4]. Studies by Fusaro [5] showed that oxygen and moisture have a detrimental effect on transfer film morphology and rheology, leading to lubricant failure. Others have shown that chemical changes like oxygen substitution into the MoS_2 lattice can also degrade friction performance [6, 7]. While a great deal has been learned about the reactions of MoS_2, oxygen and water, the mechanisms for loss of low friction and decreased wear life of MoS_2 in humid air are still largely unknown [2].

In the past two decades, a new class of metal-doped, MoS_2-based coatings has been developed that exhibit the same low friction, but improved endurance, relative to undoped MoS_2 coatings. The coatings, produced by energetic beam deposition processes, are composed of Mo + S + a metal (Ni, Au, Pb, Sn, Cr, Ti, etc.) [8–13] or metal oxides (PbO, Sb_2O_3) [14, 15]. Unlike MoS_2 coatings, which can possess strong texturing and order [16, 17], the metal doping disrupts the MoS_2 crystallite growth and the resulting coatings are typically x-ray amorphous [10]. Despite the difference in microstructure, the friction performance of these coatings is very similar to MoS_2 in dry sliding due to crystallization of MoS_2 on worn surfaces [10, 18, 19]. However, the metal doping can significantly reduce the wear rate of the coatings [18], which does not appear to be simply a result of the reduced crystallinity [20]. Importantly, some metal-doped coatings perform exceptionally well in humid environments (e.g., Ti-doped MoS_2 [12]).

One way to develop an understanding of how coating compositional and microstructural changes contribute to solid lubricant performance is through analyzing the third body processes involved in sliding, identified by Godet and colleagues as velocity accommodation modes [21–23]. Numerous ex situ studies of worn surfaces have demonstrated significant in-contact materials processing during sliding (oxidation, microstructural transformation, debris formation and ejection, etc.) [24–26]. In situ tribometry techniques can add to our understanding of *how* these changes impact tribological response of solid lubricants [27–33]. In our laboratory, we have implemented optical in situ tribometry to examine the third bodies formed in the contact and how their morphology, motion, and properties impact friction, wear and endurance [33–38]. These various optical in situ studies of boric acid [33], Pb–Mo–S, diamond-like carbon [34–36], MoS_2 [38, 39], and nanocomposite [37] solid lubricants have given direct evidence for the role of the third body in friction behavior [38].

The purpose of this article is to demonstrate that the sliding friction behavior of a Pb–Mo–S coating in dry and ambient humidity air can be explained by third body processes and velocity accommodation modes. Reciprocating sliding tests were performed with an in situ tribometer that allowed real-time visualization and Raman analysis of the sliding contact through a transparent hemisphere. Third bodies and velocity accommodation modes were identified and correlated with friction behavior in dry and ambient air. In particular, reversible deformation modes of third bodies during humid air sliding are described. The well-known rise in the friction coefficient of MoS_2 in humid air [1, 2] is analyzed in terms of two velocity accommodation modes—interfacial sliding and debris shearing—and accounted for by a model of third body friction.

2 Experimental

A 320 nm thick Pb–Mo–S coating was deposited onto a M50 hardened steel substrate (E_s = 206 GPa, ν = 0.3) by Ion Beam Deposition (IBD); details of the deposition conditions have been described previously [10]. Briefly, the coating was amorphous (by XRD and TEM) and contained 12–15 at.% Pb as determined by Rutherford Backscattering Spectroscopy (RBS). This coating was selected as representative of numerous Pb–Mo–S coatings deposited and studied in both unidirectional and reciprocating sliding [10, 18].

Visualization studies were performed with a home-built tribometer [33] whose sliding stage sits beneath an optical microscope attached to a Raman spectrometer. The tribometer was enclosed in a glove bag to control the humidity of the air. Sliding experiments were conducted by reciprocating the coated substrate underneath a stationary, transparent hemispherical counterface. Friction forces were monitored through a piezoelectric sensor in the stage under the coated sample. Counterfaces were either 12.5 mm diameter borosilicate glass (E = 64 GPa, ν = 0.2) or 6.37 mm diameter sapphire (E = 400 GPa, ν = 0.22) hemispheres. Normal loads, L = 6.37 and L = 23.9 N were used, corresponding to a mean Hertzian contact pressures between P_H = 0.48 and 1.43 GPa [40]. Each test was run at 1mm/s sliding speed over an initial track length of 6 mm, then reduced to 4 mm [41].

A total of 15 reciprocating sliding tests were run from 300 to 2,000 cycles in air, either at constant humidity (ambient air or dry air) or under "variable humidity." Ambient tests were run under laboratory conditions (45–50% RH). Dry air (RH between 1% and 4%) was supplied to the glove bag by passing pressurized air through desiccators in series with cold traps chilled with a dry ice + propanol mixture (–77 °C; partial pressure water vapor 0.08 Pa). Variable humidity tests were begun in dry air, and then humid air (48–65% RH) was added after a selected number of sliding cycles. In some of the experiments (labeled DH, for Dry-then-Humid), tests were finished in humid air; in others, labeled DHD, the humid air flow was halted and the tests were completed in dry air. Humidity was recorded continuously during experiments with an electronic hygrometer, whose precision was about 1%.

Optical microscopy was performed with white light using either a 20× or an ultralong working distance 50× objective and recorded with a CCD camera onto VHS or S-VHS tape at 30 frames/s. The video was recorded continuously except during Raman spectra acquisition, which uses the same optical path as the CCD camera. Later, a video capture card was used to obtain selected single-frame images and video clips. Optical interference between the transparent hemisphere and the coated flat resulted in Newton's rings. Destructive interference is seen for separations, h, where $h = 0$ and $h = n\lambda/2$ for integer values of n and the wavelength of light used for illumination. The diameter of the contact zone, $2a$, before sliding was measured with a calibration grating; the contact zone was seen as a dark circle, due to destructive interference. From the contact zone size and applied load, the measured contact pressure can be computed. The motion of debris in the sliding contact was studied by capturing images from videotapes played frame-by-frame. Table 1 lists the environment and contact conditions for the 15 tests reported.

Micro-Raman spectra were obtained in situ during selected cycles, usually requiring 5–20 cycles. Unfortunately, Raman peaks from sapphire hemispheres overlap the main MoS_2 Raman peaks between 200 and 300 cm^{-1}. To better resolve the MoS_2 peaks, a glass hemisphere was

Table 1 Test and tribo-contact conditions for the 15 tests reported. Contact pressure (cycle 0) computed from measured contact radius and calculated from Hertz model using the reduced modulus, E_r

Test	Measured						Computed		Calculated	
	Constant humidity tests									
	%RH	Load (N)	R (mm)	2a (μm)	μ max	μ min	E_r (GPa)	P (GPa)	$2a_H$ (μm)	P_H (GPa)
D1	1–4	6.37	6.35	191	0.08	0.07	52	0.22	168	0.29
D2	1–4	6.37	6.35	189	0.12	0.08	52	0.23	168	0.29
D3	1–4	23.9	6.35	272	0.05	0.04	52	0.41	260	0.45
D4	1–4	23.9	6.35	288	0.06	0.04	52	0.37	260	0.45
D5	<1	23.9	6.35	270	0.04	0.03	52	0.42	260	0.45
D6	<1	23.9	3.18	148	0.02	0.02	148	1.39	146	1.44
A1	45	23.9	6.35	278	0.14	0.12	52	0.39	260	0.45
A2	46	23.9	3.18	152	0.04	0.05	148	1.32	146	1.44
A3	48	23.9	3.18	150	0.05	0.05	148	1.35	146	1.44

Test	Variable humidity tests									
	RH Change	Load (N)	R (mm)	2a (μm)	μ dry	μ moist[a]	E_r (GPa)	P (GPa)	$2a_H$ (μm)	P_H (GPa)
DHD1	Step: 1% ➔ 55%	23.9	6.35	267	0.04	0.18	52	0.43	260	0.45
DHD2	Step: 1% ➔ 52%	23.9	6.35	264	0.05	0.20	52	0.44	260	0.45
DHD3	Step: 1% ➔ 48%	23.9	6.35	258	0.03	0.20	52	0.46	260	0.45
DH1	Step: 1% ➔ 61%	23.9	3.18	145	0.02	0.07	148	1.45	146	1.44
DH2	Increments[b]	23.9	6.35	271	0.04	0.12	52	0.41	260	0.45
DH3	Step: 1% ➔ 61%	23.9	6.35	275	0.03	0.18	52	0.40	260	0.45

[a] Maximum friction coefficient in moist air

[b] After 450 cycles at RH < 1%, the RH was raised by 5% every ~100 cycles up to 55% over 1,000 cycles

used for some experiments; MoS_2 spectra can be resolved even though they are located on a broad background from the amorphous glass. For reference, Fig. 1 shows Raman spectra of (a) crystalline MoS_2 obtained through a glass hemisphere, (b) the glass hemisphere, (c) crystalline MoS_2, and (d) the as-deposited Pb–Mo–S coating. After sliding, contacts were separated and micro-Raman analysis was performed ex situ on wear track and hemisphere surfaces.

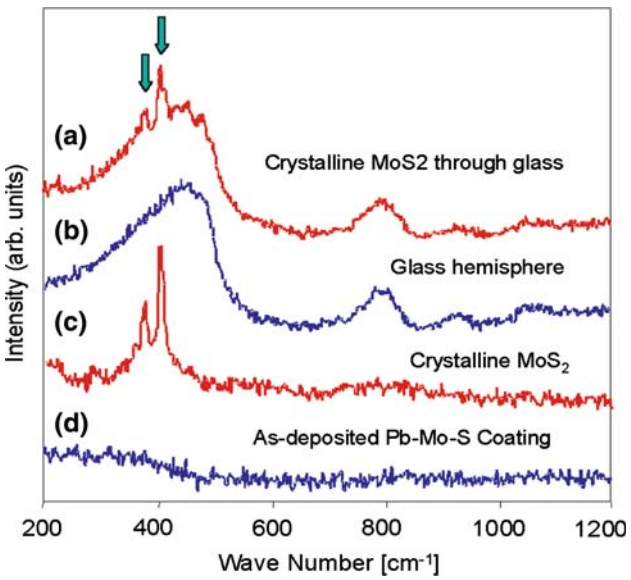

Fig. 1 Reference Raman spectra for Pb–Mo–S coating, MoS_2, glass hemisphere, and crystalline MoS_2 obtained through the glass hemisphere

3 Results

3.1 Friction Behavior

Figures 2 and 3 show selected friction coefficient versus cycle curves in dry (RH < 1–4%) and ambient (RH ~ 45%) air for three initial contact stresses ranging from 0.2 to 1.4 GPa. In both dry and ambient air, the friction coefficient started at about 0.1–0.2 then fell during run-in to a "nominally" steady value. We say "nominally" because after run-in, the friction coefficient often exhibited a rise from 5% to 20% above the run-in friction minimum before approaching a steady-state value. Table 1 summarizes high and low steady-state friction coefficients for the two counterfaces in constant and variable humidity tests. Under identical stresses, the friction coefficients in ambient

air were from 2 to 4 times higher than in dry air. Moreover, the friction coefficient decreased with increasing contact stress in both dry and ambient air; this is consistent with our earlier ex situ studies of Pb–Mo–S in dry air [10].

Figure 4 shows friction coefficient versus cycle curves along with humidity versus cycle curves from three variable humidity tests. The bottom curve shows that the friction coefficient rose sharply with a step increase in humidity, but then dropped as sliding continued in humid air. The drop in humid air was seen in 4 of the 5 humidity step tests (DHD2, DHD3, DH1, DH3), regardless of the cycle at which the humidity was increased (from 300 cycles to 1,000 cycles). The exception (test DHD1), seen in the middle graph of Fig. 4, had constant friction coefficient during elevated humidity stage of the test. In all five tests, however, the friction coefficient rose by a factor of 4–7 going from dry to humid air. We note this is about twice the magnitude of the friction difference between single-environment tests (dry or ambient), where friction coefficients differed by a factor of 2–4. However, during humid sliding, the ratio of final friction coefficients (ambient/dry) was about 2.5–3, consistent with the ratio of ambient/dry friction observed in constant environment tests. Finally, in all 3 DHD tests, the friction coefficient dropped to its initial (low steady-state) value when the humid air was replaced by dry air.

The upper graph in Fig. 4 depicts friction and humidity curves for an incremental step-humidity test, DH2; here the humidity was increased in steps of 5%, from <1% to 55%, roughly every 100 cycles, after 450 cycles of dry sliding to run-in the contact. In this test, the friction coefficient increased by only a factor of 3, approximately the factor found in constant humidity stress tests. The graph also shows that the friction coefficient began to fall at RH values above 51% even as the RH increased. Test DH3, with a step increase in RH to 61% also had a similar drop in the friction coefficient at about 45% RH (not shown), but DH1 with a similar step increase, did not show a drop in the friction coefficient before 61% RH was reached.

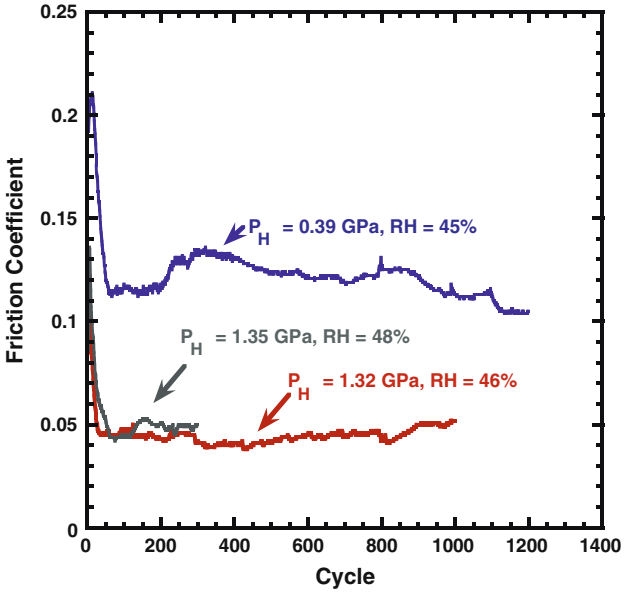

Fig. 3 Friction coefficient versus cycle curves for tests A1, A2, and A3 run in ambient air at low and high contact stress

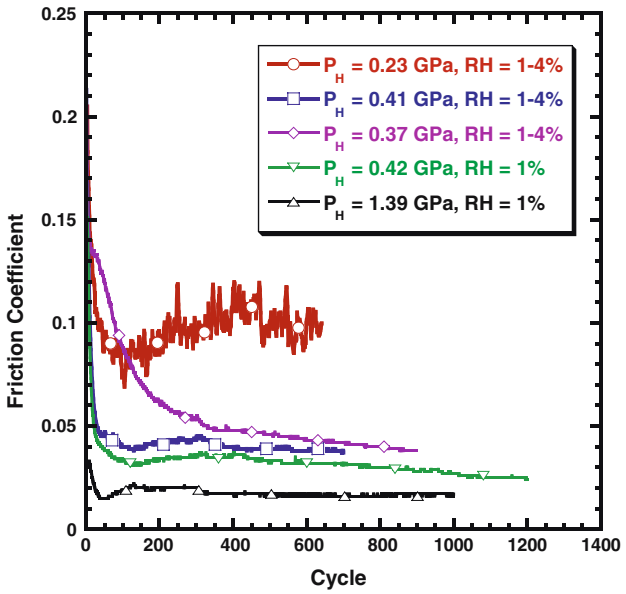

Fig. 2 Friction coefficient versus cycle curves for tests D2–D6 run in dry air at a range of contact stress

3.2 In Situ Tribometry and Raman Analysis

3.2.1 Dry Air Sliding

Images of the contact taken before sliding showed Newton's rings. The apparent area of contact (dark circle in the center) remained constant during run in and well into steady-state sliding. During run in, third bodies generated in the sliding contact gradually accumulated on the hemisphere and agglomerated as a thin transfer film; those at the edges and outside of the contact became compact and loose debris. Evolution of the third body morphology is consistent with earlier ex situ studies of Pb–Mo–S coatings, in which tests were interrupted and the contacts separated and analyzed [10, 18].

Figure 5 shows three in situ images captured from a video recording during cycles 80, 500, and 870 of test D4. At cycle 80, at the end of run-in, the central area of contact had a diameter of 270 μm; this value is within 2% of the diameter predicted by Hertz contact calculations. Measured

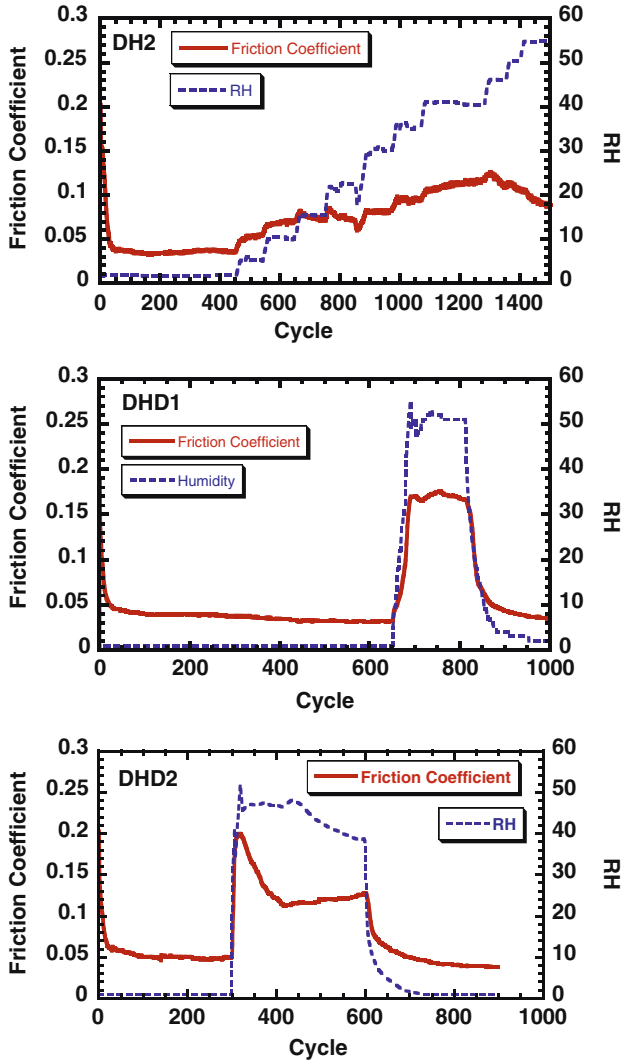

Fig. 4 Friction coefficient and relative humidity versus cycle for tests DH2 (top), DHD1 (middle), and DHD2 (bottom)

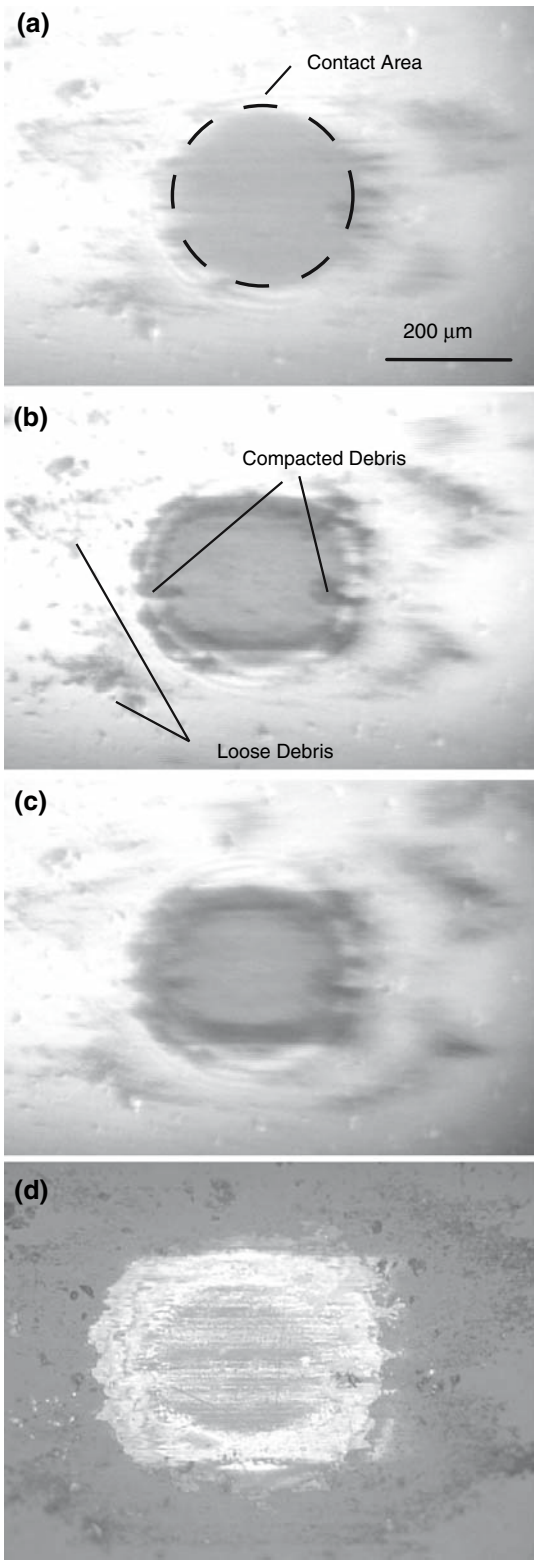

Fig. 5 Three in situ images captured from a video recording during cycles (**a**) 80, (**b**) 500, and (**c**) 870 of test D4. Ex situ image of contact after test D4 (**d**)

contact diameters from this and other tests were from 1% to 11% larger than the calculated values (see Table 1). Figure 5a also shows that compacted debris collected at the left and right edges of the contact, as expected in reciprocating sliding, and loose debris outside the contact. Video analysis showed that both the compacted and loose debris remained stationary on the hemisphere during sliding.

Images of the contact after 500 and 870 cycles, Fig. 5b, c, looked remarkably similar to the contact after 80 cycles, except that the hemisphere had accumulated more debris. This behavior was seen in all dry sliding tests: as sliding continued, the transfer film thickened while more compacted and loose debris collected in and around the contact. Occasionally, debris fell off the hemisphere onto the track, where it stuck, and could be seen moving through the contact at the test speed (1 mm/s). Other times, debris from the track would re-attach to the hemisphere, both inside and outside the contact. However, most of the time, the

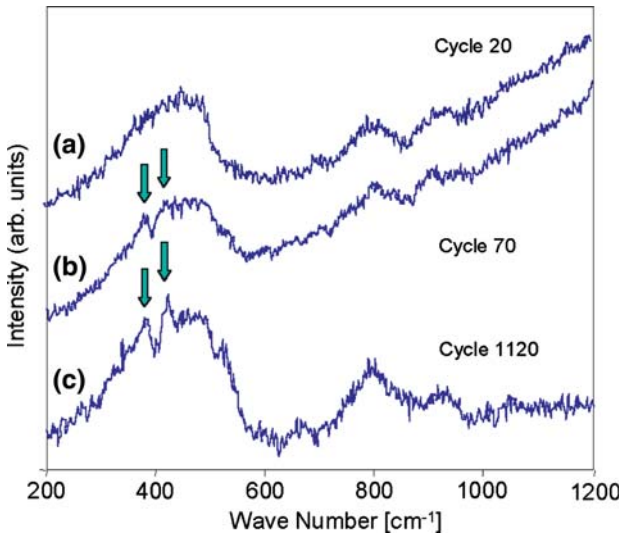

Fig. 6 In situ Raman spectra taken during a friction test in dry air

third bodies were stationary with respect to the hemisphere, indicating that they adhered securely to the counterface. The ex situ image (d) of the transfer film is consistent with the in situ observations. These in situ observations demonstrate that the velocity accommodation mode in dry air was predominantly interfacial sliding.

Figure 6 shows Raman spectra obtained in situ during a dry sliding test. The only peaks seen in spectrum (a), recorded during run-in (cycles 12–33), are from the glass hemisphere (and presumably the amorphous Pb–Mo–S coating). Spectrum (b), recorded after run-in (cycles 66–87), shows the emergence of two peaks (around 400 cm^{-1}) characteristic of MoS_2. Spectrum (c), recorded in steady state during cycles 1,108–1,141, shows stronger MoS_2 peaks. No peaks other than those associated with MoS_2 were observed. Ex situ optical microscopy showed an adherent transfer film on the hemisphere, and ex situ Raman spectra showed similar (but always more intense) MoS_2 peaks, both in the transfer film and on the wear track (not shown), consistent with previous ex situ studies [10, 18].

3.2.2 *Ambient Humidity Air Sliding*

Videos taken early (5–10 cycles) in the ambient humidity (45%) test, when the friction coefficient was highest (not shown), showed very little transfer film adhering to the counterface. Debris particles were seen on the wear track, and temporarily in the contact, before being extruded and ejected. As the friction coefficient fell, some debris adhered to the hemisphere, while other debris adhered to the wear track. Gradually, a transfer film similar to the dry sliding film built up on the hemisphere (See Fig. 7, cycle 30, test A1). But, unlike the dry sliding case, the film continued to thicken and coarsen with continued sliding (Fig. 7, cycles 90, 500, and 1,010). The coarsening was due to inhomogeneity in the film thickness, identified by contrast and transparency changes.

All tests run in ambient air showed interfacial sliding between the transfer film and the track to be the dominant velocity accommodation mode, as was the case in dry air. However, a second velocity accommodation mode—debris shearing—was also seen in ambient sliding tests. In the low contact-stress test, A1, patches of debris appeared to be extruded back and forth early in steady-state sliding. In the high contact-stress tests, A2 and A3, this debris movement was delayed. For example, in test A3, debris movement began about cycle 100, as the friction coefficient began to rise, whereas in test A1, debris movement began between 10 and 20 cycles.

An example of the second velocity accommodation mode is shown in Fig. 8, which shows a sequence of five images taken during cycle 68 of test A1. It illustrates not only debris movement but, additionally, the reversibility of the process during one reciprocating sliding cycle. The five images, captured from videotape, were taken at roughly equal intervals as the contact traveled 6 mm from the right end of the track, to the left end, then back to the right end. An ellipse encloses several patches of debris that traversed about 80 microns across the contact zone—first to the right, then to the left—during the cycle. During the traverse, the patches contracted half way down the track then expanded as the hemisphere reached the turn around spot. Later in sliding, between cycles 100 and 300 in test A1, larger patches of debris could be seen moving back and forth. From the video, we observed that the top of the patch in contact with the hemisphere moved in the same direction as the bottom of the patch in contact with the track. However, the bottom of the patch moved a larger distance than the top of the patch. We call this motion "reversible

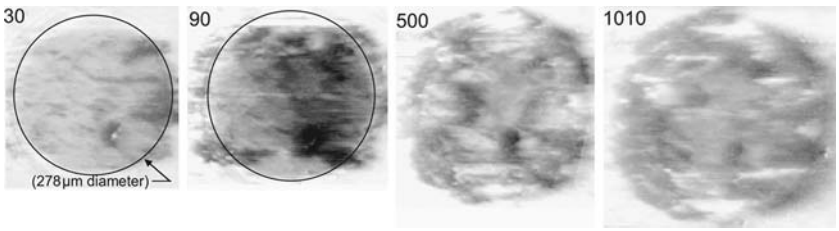

Fig. 7 In situ images of transfer films during ambient sliding (test A1) showing, thickening, and coarsening of the transfer film

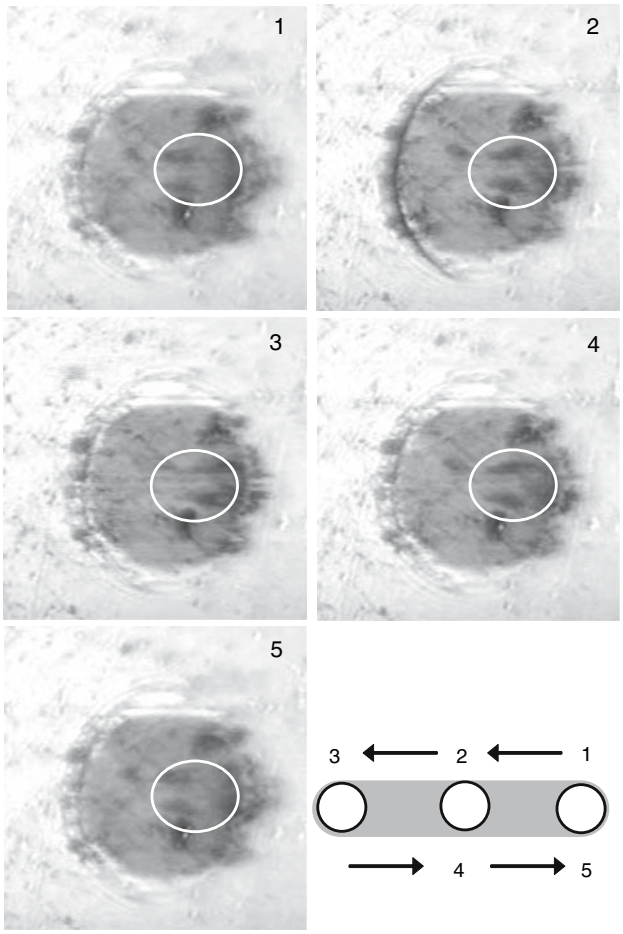

Fig. 8 Five images taken at roughly uniform intervals as the contact traveled 6 mm from the right end of the track, to the left end, then back to the right end (i.e., the substrate moved right then returned left). The ellipse shows two patches of debris that traversed about 80 microns—first to the right, then to the left—during cycle 68 of test A1. Schematic (lower right) indicates position of contact relative to track

extrusion." Reversible extrusion continued even as the transfer film coarsened, As the transfer film became more inhomogeneous, small and large patches of debris exhibited reversible extrusion, the smaller events occurring around what appeared to be pits in the transfer film.

Similar examples of reversible extrusion were found in all tests run in humid air. These deformation events were observed both inside the contact and at the periphery of the contact, where debris captured from the track and debris extruded from the transfer film accumulated. A consequence of reversible extrusion was that even though regions of the transfer films were continuously being deformed, the accumulated deformation over 10 and 100 s of cycles was small. This hysteretic effect explains why images observed cycle-by-cycle did not reveal changes in transfer film morphology. In fact, the biggest change in appearance of the transfer film over hundreds of cycles was the increasing accumulation of debris. We note additionally that the spatially resolved friction data (friction coefficient along the track) was nearly constant during each cycle (not shown), which is consistent with the uniform hysteresis seen in the debris motion.

In situ Raman spectroscopy also confirmed the evolution and presence of MoS_2 during all ambient sliding tests (not shown). Moreover, no evidence for a second Raman-active compound, MoO_3 could be found. Ex situ Raman analysis confirmed the presence of MoS_2 on both the wear track and in the transfer film and the absence of MoO_3 or other possible Raman-active compounds like MoO_2 and $PbMoO_4$ [15]. Ex situ optical analysis of the wear track showed increased debris accumulation in ambient sliding tests although the wear tracks were not significantly deeper after 2,000 cycles.

3.2.3 Variable Humidity Tests: Dry/Humid/Dry Air Sliding

For these experiments (DHD1-3), the appearance of the transfer films during and after the humidity exposure did not change significantly, other than the continued accumulation of third body debris (not shown). Furthermore, images examined cycle by cycle during the humidity/friction transitions also did not show significant changes, suggesting that the morphology of the transfer film did not change during rapid rises or falls in humidity. However, examination of video images taken along a single traverse during humid sliding again revealed deformation of some debris particles within the transfer film. The motion began as the humidity and friction coefficient rose, continued during the higher humidity stage, then declined as the humidity and friction coefficient fell.

Figure 9 shows a sequence of 5 images taken during cycle 695 of test DHD1, in the middle of the high humidity stage (friction data shown in Fig. 4). The images, from top (1) to bottom (5), were taken at 0.8 mm (0.8 s) intervals during a 4 mm traverse of the track from left to right. Two regions where debris particles moved relative to the hemisphere are outlined by circles and boxes, respectively. The circled region shows debris accumulating (1, 2), moving to the right (3), then extruding into a broad patch (4, 5). The boxed region shows debris (1) moving to the right (2), then extruding into a shape that resembles a sideways 'U' before exiting the box; the motion of the debris is reversed on the return traversal. Here too, during humid air sliding of a transfer film formed initially in dry air, we see third-body motion suggesting that patches of debris in the transfer film underwent shear, and were extruded, in the contact. This extrusion was also reversible (not shown).

In situ Raman spectra in Fig. 10 shows that MoS_2 was formed in the contact during dry sliding and persisted during all three stages of test DHD1: No MoS_2 peaks were seen early in sliding, (a), but appeared after about 300 cycles. We note there are subtle changes in the background spectra occurring between spectra (a) and (e). These changes do not appear to be the result of oxide formation [15]. It is possible that small changes in transfer film thickness shift the position of the hemisphere relative to the focus point of the Raman microscope, resulting in subtle change in the relative contribution of the glass background and signal from the transfer film itself. The spectra taken at RH = 50% (d) were identical with those at RH < 2%, before (c) and after (e) the high humidity stage. Moreover, no evidence for any other Raman-active compounds could be found. Ex situ Raman analysis confirmed the presence of MoS_2 on both the wear track and in the transfer film and the absence of MoO_3 and other oxides (not shown).

Step humidity tests showed similar third body behaviors to the variable humidity tests. Both showed a friction rise, then slow decrease, after increasing humidity, as well as reversible extrusion events. In some cases, the extrusion distances fell as the friction coefficient dropped; in other cases, the extrusion distance remained the same, only to change as the transfer film coarsened. In situ analysis of the incremental humidity step test, DH2, found that the extrusion distance increased with increasing humidity, but as the transfer film coarsened, the extent and amount of reversible extrusion decreased.

4 Discussion

In situ tribometry revealed the third body processes (buildup, attachment, and shearing) and third body composition changes ('amorphous' to MoS_2-like) that occurred at the buried interface during sliding. It also identified changes in velocity accommodation associated with an increase in friction when the environment was changed from dry to humid air. For both dry and humid conditions, the most prominent third body seen was a transfer film, containing MoS_2 that formed on the hemisphere. As the transfer film built up during run-in, friction dropped. In dry air, the transfer film remained stationary on the hemisphere and sliding motion took place at the interface along the stationary transfer film and the wear track. In humid air, the velocity was accommodated mainly by interfacial sliding, although some of the motion was accommodated by shear/extrusion of patches of debris within the transfer film. Deformations in this 2nd velocity accommodation mode were reversible, leading to virtually no change in appearance of the transfer film over a cycle of sliding. Thus the

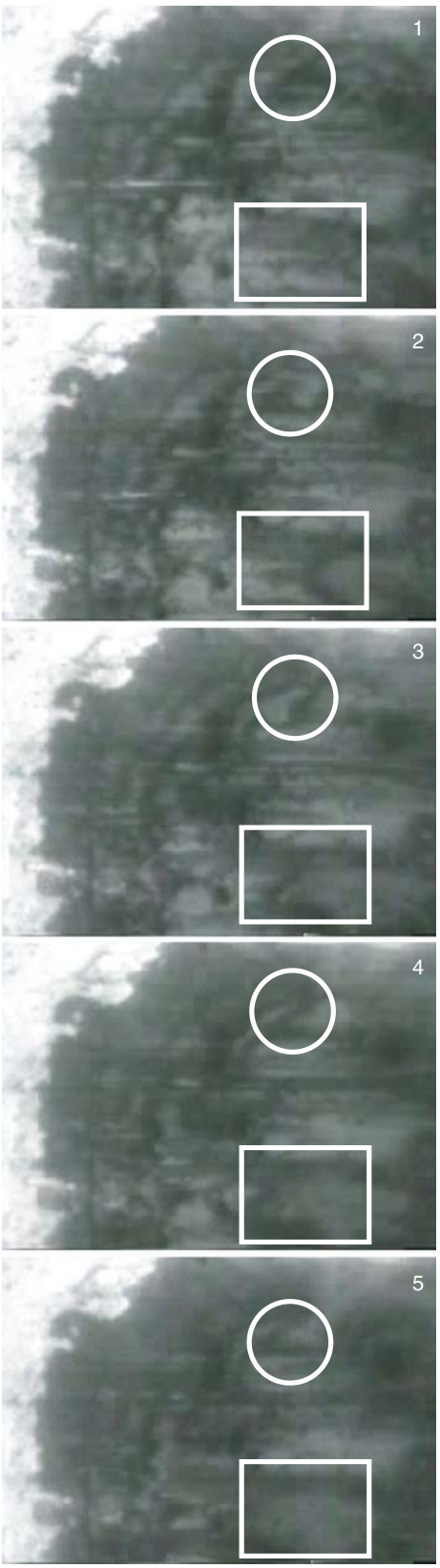

Fig. 9 A sequence of 5 images taken 0.8 mm apart during cycle 695 of test DHD1, in the middle of the high humidity stage. Substrate moved from left to right

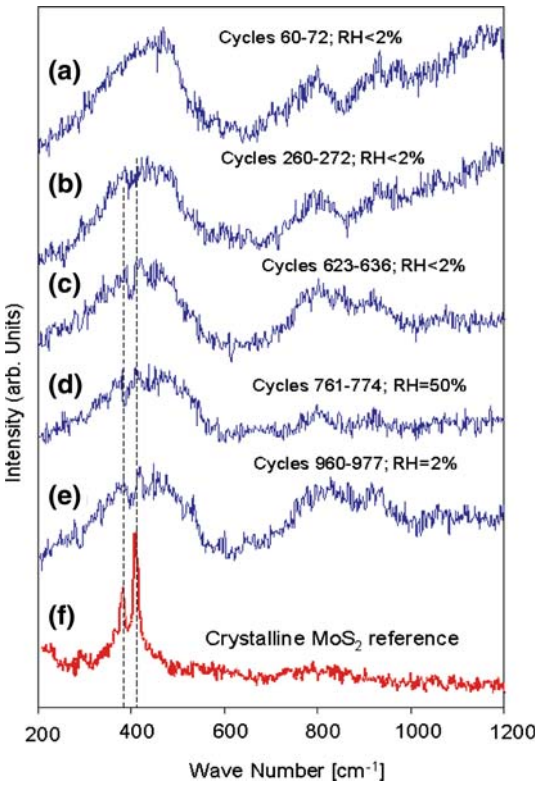

Fig. 10 In situ Raman spectra from test DHD1

dominant velocity accommodation mode in both dry and ambient air was interfacial sliding.

In situ Raman spectroscopy verified that the transfer film generated from amorphous Pb–Mo–S contained MoS_2. Raman did not detect MoS_2 during the run-in stage. Presumably, the material removed from the track at the beginning of sliding was either amorphous or too thin to be detected. But soon after run-in, MoS_2 was identified in the transfer film. This direct evidence that MoS_2 *formed inside* the contact during sliding confirms earlier inferences from ex situ studies with Raman spectroscopy on Pb–Mo–S [10] and similar Mo–S based coatings [14, 15]. Previous structural studies of Pb–Mo–S transfer films and wear tracks, using high resolution transmission electron microscopy, have identified nanocrystalline MoS_2 in debris and on wear track surfaces [18]. Thus the compositions of the surfaces in sliding contact, after run in, are clearly a MoS_2 transfer film against a wear track surface, also containing MoS_2. Taken together, the low friction in dry air can be directly attributed to interfacial sliding between a MoS_2 transfer film on the hemisphere and the MoS_2-containing wear track surface.

At higher humidity (45–50% RH), MoS_2 was also formed in the sliding contact. Raman did not detect MoO_3, a strong Raman scatterer, nor any other known Raman active phases (e.g., MoO_2, PbO_2, or $PbMoO_4$), suggesting that the transfer film remained mainly MoS_2 in ambient air. Therefore, it is likely that the particles undergoing shear/extrusion in humid air were MoS_2 particles.

In both dry and humid air, the friction coefficient depended on humidity and load. In dry air, the friction coefficients were much lower (factor of 4–8) than in humid air. We can account for these differences with a two term friction model describing the third body behavior. The model makes the simplifying assumption, as does the Bowden and Tabor (BT) two body friction model [42], that the friction coefficient, μ, can be found by adding together an interfacial friction term, μ_{int} and a shearing term, μ_{shear}:

$$\mu = \mu_{\text{int}} + \mu_{\text{shear}} \tag{1}$$

Like the two body models, μ_{int} depends on an interfacial shear strength S_{int}, and μ_{shear} depends on a shearing term S_{debris}. In the third body model, the former term describes the interfacial shear strength between the debris and the track and the latter term, the shear strength of the debris (not that of the coating). In what follows, we will present a semi-quantitative, three body model for the friction coefficient as a function of load and humidity.

In dry air, interfacial sliding was the only velocity accommodation mode contributing to the friction coefficient. Since debris shearing was never observed, $\mu^{\text{d}}_{\text{shear}} = 0$ (where the superscript "d" refers to the dry air condition). Hence, the friction coefficient in dry air, by Eq. 1, $\mu^{\text{d}} = \mu^{\text{d}}_{\text{int}}$. The absence of debris shear in dry air suggests that the shear strength of the debris formed in dry sliding was greater than the interfacial shear strength, i.e., $S^{\text{d}}_{\text{debris}} > S^{\text{d}}_{\text{int}}$, i.e., the force transmitted across the sliding contact was insufficient to deform the transfer film. This inference is consistent with the results of Uemura et al. [43] who have shown that the shear strength of MoS_2 crystallites was 2–3 times greater than the interfacial shear strength of MoS_2 sliding against MoS_2 in dry air.

We also found that the variation in friction with load is consistent with "Hertzian" friction behavior [44]. This behavior is well described by the simple relationship

$$\mu^{\text{d}}_{\text{int}} = S^{\text{d}}_{\text{int}}/P_H \tag{2}$$

where P_{H} is the mean Hertzian pressure in the contact [40] and $S^{\text{d}}_{\text{int}}$ is the interfacial shear strength. For many solid lubricated interfaces, and in particular MoS_2 [44], the interfacial shear strength has been shown to follow [45]

$$S_{\text{int}} = S_0 + \alpha P_{\text{H}} \tag{3}$$

where S_0 and α are the pressure-independent and pressure-dependent contributions to the shear strength. The interfacial shear strength parameter, S_{int}, can be calculated from the material properties and initial contact radii given in

Table 1. By linear least squares fitting the steady-state friction coefficients in dry air versus $1/P_H$, we get $S_0^d = 16.5 + 0.2$ MPa and $\alpha = 0.000 \pm 0.006$ (zero, within error); the fit is plotted as a thick line in Fig. 11. This value is consistent with previously reported interfacial shear strengths for Pb–Mo–S [10] and MoS_2 [44] of $8 < S_0^d < 23$ MPa in dry air.

By contrast, in humid air, the higher friction coefficients were accompanied by both interfacial sliding and debris shearing/extrusion, with interfacial sliding being the primary velocity accommodation mode. Therefore, the friction coefficient requires both interfacial and debris shearing/extrusion terms: $\mu^h = \mu_{int}^h + \mu_{shear}^h$ (superscript "h" designates humid air). The contribution of debris shearing signifies that, at some patches of transfer film, the applied shear stress exceeded the shear strength of debris. Nonetheless, the interfacial sliding term μ_{int}^h was the dominant contribution to friction, which allows us to approximate $\mu_{int}^h \approx \mu_{int}^h = S_{int}^h/P_H$. Again we perform a linear least squares fit, this time to the constant humidity friction coefficients versus $1/P_H$, using Eq. 3 with the friction data and other parameters in Table 1, and we get $S_0^h = 39 \pm 1$ MPa and $\alpha = 0.019 \pm 0.001$ in humid air (data from constant humidity conditions, Table 1). The fit is shown as an upward-sloping thick line in Fig. 11. S_0^h in ambient air was a bit more than twice that in dry air, and $\alpha = 0.019$ in humid air indicates that the friction coefficient in 50% RH air cannot fall below $\mu^h = 0.019$ at any load.

From the above analysis, we conclude that the steady-state interfacial sliding term, μ_{int}, increased in humid air. Over these pressure ranges, we expect relative increases in interfacial shear strength, S_{int}^h/S_{int}^d of between 3 (at ~0.45 GPa) to 4 (at ~1.5 GPa) in our experiments (calculated from Eq. 2), with concomitant increases in friction (calculated from Eq. 1). However, this cannot explain how the friction coefficient in step humidity tests initially rose by 20–150% more than would be predicted by the interfacial shear strengths measured in dry and ambient air sliding (see humid air shear strengths plotted in Fig. 11, as compared to the predicted value shown by the broad line). Nor can it explain why the friction coefficient dropped in most step humidity tests.

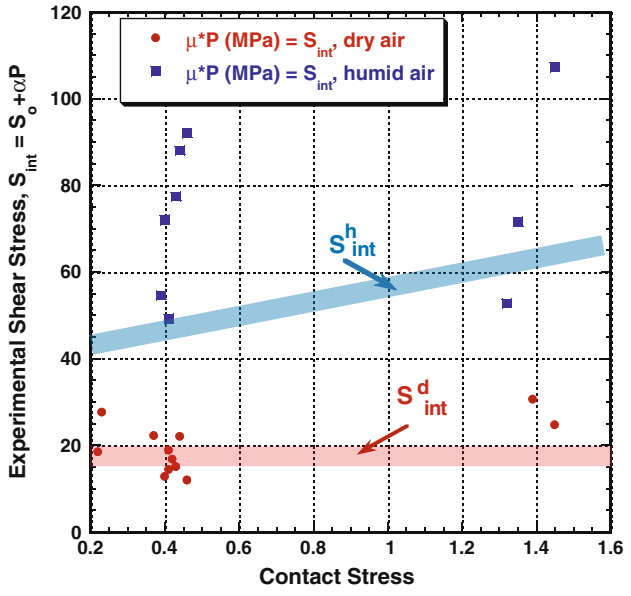

Fig. 11 Interfacial shear strengths determined by linear regression (bars, from constant humidity tests in Table 1) for dry and humid conditions; points are all data from Table 1

To explain the discrepancies where the humidity was changed rapidly, we postulate that S_{int}^h initially rose up to almost twice the constant humidity value, probably the result of surface chemical interactions of moisture on the wear track. This rise in interfacial shear strength was not *initially* accompanied by shearing of debris because the only debris in the contact was "dry" debris (formed in dry sliding) like that found by Uemura et al. [43] to be quite resistant to interfacial shearing. Over the next 50–100 cycles, two events transpired to lower the friction coefficient: First, sliding in moist air produced new third bodies and probably transformed the outer layers of the transfer film on the ball. The new third bodies, as stated earlier, clearly sheared at lower applied stress than the dry debris; hence, $S_{debris}^h < S_{debris}^d$. Secondly, the interfacial shear strength term, S_{int}^h, dropped, reflecting the decrease in friction coefficient as in the DHD2 test in Fig. 4. We speculate that the drop might have been due to one of two surface conditions: (1) either a very thin—too thin to be detected by Raman spectroscopy—and lubricious reaction film was formed, or (2) the wettability of the new interface changed, and the adsorbed water on the track modified the interfacial shear strength. While we have no direct evidence for the latter, we have previously observed strong effects of adsorbed gases on friction behavior [46]. Thus after 100 or so cycles, the interface became similar to that found in tests started at ambient humidity, thus the friction coefficients of the two became similar. When the dry air replaced humid air, the low friction coefficient was restored because only interfacial sliding occurred and the friction coefficient was again controlled by S_{int}^d.

On the basis of these arguments, we can now explain semi-quantitatively the effect of humidity on the friction behavior of Pb–Mo–S. In variable humidity tests DHD and DH, where the debris were formed initially in dry air, the friction coefficient could rise a factor of 4–8 because the "dry" debris were very resistant to shear. Thus S_{int}^h, the initial shear strength of the debris/wear track interface could be greater than the calculated steady state value, $S^h = 39$ MPa + 0.019 P_H.

As sliding continued, new debris were formed at the moisture-exposed wear track. Having a lower shear strength than the dry debris, they began to shear and as a consequence, the friction coefficient fell (in all but test DHD2) to values comparable to the steady state friction coefficient in ambient air. These debris, like those formed from the beginning in ambient air, were generated in humid air and as might be expected would have different shear properties than debris generated in dry air. In particular, the drop in friction coefficient and the onset of shear/extrusion indicates that $S^{h}_{debris} < S^{d}_{int}$. Hence, the friction coefficient in humid air will be limited by S^{h}_{debris}.

A similar argument can be given to account for the rise then drop in friction coefficient in tests conducted above 51% RH. Again, we hypothesize that the friction coefficient was the result of a competitive process: the interfacial shear strength rose commensurate with increasing RH, causing S^{h}_{int} and the friction coefficient to rise; but at high humidity, the ongoing drop in shear strength S^{d}_{debris} of humid-formed debris reduced the friction coefficient. This competition, of course, developed slowly. At a time scale of one cycle (12 or 8 s), neither the interfacial shear term S_{int}, which drives debris shearing, nor the debris shear strength S_{debris} varied rapidly. Thus, the reversible extrusion can be accounted for by the constancy of the interfacial shear stress over the time needed to complete one cycle. By contrast, in step tests, the S_{int} value changes rapidly with RH, but S_{debris} does not, which accounts for the time dependence in both the friction coefficient and the delayed shear/extrusion.

5 Summary

1. The MoS_2 transfer film formed during the initial run-in against a Pb–Mo–S coating is responsible for the low friction coefficients achieved in dry and humid air.
2. The velocity accommodation mode under both dry and humid sliding conditions was primarily interfacial sliding. A second mode, transfer film shearing, was also observed during humid air sliding.
3. The friction coefficient in dry sliding is controlled solely by interfacial sliding and can be calculated in terms of the interfacial shear strength and the elastic (Hertz) contact pressure.
4. The friction coefficient in humid air has two contributions:
   a. an interfacial sliding contribution (μ^{h}_{int}) shown here to be greater than μ^{d}_{int}.
   b. a shearing contribution (μ^{h}_{shear}) which depends on the shear strength of the third body, here seen as the transfer film or patches of debris in the transfer film.
5. The second velocity accommodation mode seen in humid air is attributed to shearing of debris that forms and is likely softened in humid air. As the shear strength of 'humidity-formed' debris falls below the shear stress transmitted by interfacial sliding, the debris begins to shear.
6. The friction coefficient in humid air depends on both contact pressure and S^{h}_{int}.
7. The reversibility of this shear/extrusion process is attributed to the near constant interfacial friction term (i.e., interfacial shear stress) during each cycle.

6 Conclusions

In situ microscopy identified third body processes and velocity accommodation modes associated with the sliding friction behavior of amorphous Pb–Mo–S coatings in dry and ambient humidity. The main third body observed was a transfer film that formed on the stationary hemisphere during run-in; the only compound in the transfer film, as identified by in situ Raman spectroscopy, was MoS_2. The dominant velocity accommodation mode in dry and humid air was interfacial sliding between the outer surface of the transfer film and the wear track; this interface, based on present and earlier studies, is nanocrystalline MoS_2. Therefore, the friction coefficient was controlled by a velocity accommodation parameter, the interfacial shear strength of MoS_2 sliding against MoS_2. The rise in the friction coefficient from around 0.04 in dry air to around 0.15 in humid air produced a small but observable second velocity accommodation mode, shear/extrusion of the transfer film, which appeared reversible in reciprocating sliding tests. It is concluded that the friction rise in humid air was primarily due to an increase in the interfacial shear strength, and that the rise in friction caused the third body to deform rather than the deformation causing the friction to rise.

Acknowledgments The authors are grateful for support through NRL and the Office of Naval Research. This research was performed while one of the authors (SDD) was at NRL on an ASEE Postdoctoral Associateship.

References

1. Winer, W.O.: Molybdenum disulfide as a lubricant: a review of the fundamental knowledge. Wear **10**, 422–452 (1967)
2. Lansdowne, A.R.: Molybdenum disulphide lubrication. Elsevier, Amsterdam (1999)
3. Neiderhäuser, P., Hintermann, H.E., Maillat, M.: Moisture-resistant MoS_2-based composite lubricant films. Thin Solid Films **108**, 209–218 (1983)
4. Pritchard, C., Midgley, J.W.: Effect of humidity on friction and life of unbonded molybdenum disulphide films. Wear **13**, 39–50 (1969)

5. Fusaro, R.L.: Lubrication and failure mechanisms of molybdenum disulfide films. I. Effect of atmosphere. NASA, Cleveland, OH (1978)
6. Fleischauer, P.D., Lince, J.R.: A comparison of oxidation and oxygen substitution in MoS_2 solid film lubricants. Tribol. Int. **32**, 627–636 (1999)
7. Donnet C., Martin J.M., LeMogne T., Belin M.: Super-low friction of MoS_2 coatings in various environments. Tribol. Int. 29, 123–128 (1996)
8. Stupp, B.C.: Synergistic effects of metals co-sputtered with MoS_2. Thin Solid Films **84**, 257–266 (1981)
9. Spalvins, T.: Frictional and morphological properties of Au-MoS_2 films sputtered from a compact target. Thin Solid Films **118**, 375–384 (1984)
10. Wahl, K.J., Seitzman, L.E., Bolster, R.N., Singer, I.L.: Low friction, high-endurance, ion-beam-deposited Pb-Mo-s coatings. Surf. Coat. Technol. **73**, 152–159 (1995)
11. Teer D.G., Hampshire J., Fox V., Bellido-Gonzalez V.: The tribological properties of MoS_2/metal composite coatings deposited by closed field magnetron sputtering. Surf. Coat. Technol. **94–95**, 572–577 (1997)
12. Renevier, N.M., Fox, V.C., Teer, D.G., Hampshire, J.: Coating characteristics and tribological properties of sputter-deposited MoS_2/metal composite coatings deposited by closed field unbalanced magnetron sputter ion plating. Surf. Coat. Technol. **127**, 24–37 (2000)
13. Simmonds M.C., Savan A., Pfluger E., Van Swygenhoven H.: Microstructure and tribological performance of MoS_x/Au co-sputtered composites. J. Vac. Sci. Technol. A 19, 609–613 (2001)
14. Zabinski J.S., Donley M.S., Dyhouse V.J., McDevitt N.T.: Chemical and tribological characterization of PbO–MoS_2 films grown by pulsed laser deposition. Thin Solid Films 214, 156–163 (1992)
15. McDevitt N.T., Donley M.S., Zabinski J.S.: Utilization of Raman spectroscopy in tribochemistry studies. Wear 166, 65–72 (1993)
16. Seitzman, L.E., Bolster, R.N., Singer, I.L.: X-ray diffraction of MoS_2 coatings prepared by ion-beam-assisted deposition. Surf. Coat. Technol. **52**, 93–98 (1992)
17. Seitzman, L.E., Singer, I.L., Bolster, R.N.: Effects of temperature and ion-to-atom ratio on the orientation of IBAD MoS_2 coatings. Thin Solid Films **260**, 143–147 (1995)
18. Wahl, K.J., Dunn, D.N., Singer, I.L.: Wear behavior of Pb–Mo–S solid lubricating coatings. Wear **230**, 175–183 (1999)
19. Grosseau-Poussard, J.L., Garem, H., Moine, P.: High-resolution transmission electron microscopy study of quasi-amorphous MoS_x coatings. Surf. Coat. Technol. **78**, 19–25 (1996)
20. Wahl, K.J., Dunn, D.N., Singer, I.L.: Effects of ion implantation on microstructure, endurance and wear behavior of IBAD MoS_2. Wear **237**, 1–11 (2000)
21. Godet, M.: The third-body approach: a mechanical view of wear. Wear **100**, 437–452 (1984)
22. Godet, M.: Third-bodies in tribology. Wear **136**, 29–45 (1990)
23. Berthier, Y., Godet, M., Brendle, M.: Velocity accommodation in friction. Tribol. Trans. **32**, 490–496 (1989)
24. Singer, I.L.: A thermochemical model for analyzing low wear-rate materials. Surf. Coat. Technol. **49**, 474–481 (1991)
25. Singer, I.L.: Mechanics and chemistry of solids in sliding contact. Langmuir **12**, 4486–4491 (1996)
26. Singer, I.L.: Friction, wear and third body processes. MRS Bull. **23**, 37–40 (1998)
27. Sliney, H.E.: Dynamics of solid lubrication as observed by optical microscopy. ASLE Trans. **21**, 109–117 (1977)
28. Berthier, Y., Play, D.: Wear mechanisms in oscillating bearings. Wear **75**, 369–387 (1982)
29. Belin, M., Martin, J.M.: Triboscopy, a new approach to surface degradations of thin- films. Wear **156**, 151–160 (1992)
30. Wahl, K.J., Belin, M., Singer, I.L.: A triboscopic investigation of the wear and friction of MoS_2 in a reciprocating sliding contact. Wear **214**, 212–220 (1998)
31. Jullien, A., Meurisse, M.H., Berthier, Y.: Determination of tribological history and wear through visualisation in lubricated contacts using a carbon-based composite. Wear **194**, 116–125 (1996)
32. Descartes, S.: Lubrification solide a partir d'un revetement de mosx: Conséquences de la rhéologie et des débits de troisième corps sur le frottement. INSA de Lyon, Lyon, France (1997)
33. Dvorak, S.D., Wahl, K.J., Singer, I.L.: Friction behavior of boric acid and annealed boron carbide coatings studied by in situ Raman tribometry. Tribol. Trans. **45**, 354–362 (2002)
34. Scharf, T.W., Singer, I.L.: Role of third bodies in friction behavior of diamond-like nanocomposite coatings studied by in situ tribometry. Tribol. Trans. **45**, 363–371 (2002)
35. Scharf, T.W., Singer, I.L.: Monitoring transfer films and friction instabilities with in situ Raman tribometry. Tribol. Lett. **14**, 3–8 (2003)
36. Scharf, T.W., Singer, I.L.: Quantification of the thickness of carbon transfer films using Raman tribometry. Tribol. Lett. **14**, 137–145 (2003)
37. Chromik, R.R., Baker, C.C., Voevodin, A.A., Wahl, K.J.: In situ tribometry study of lubricating nanocomposite coatings. Wear **262**, 1239–1252 (2007)
38. Singer I.L., Dvorak S.D., Wahl K.J., Scharf T.W.: Role of third bodies in friction and wear of protective coatings. J. Vac. Sci Technol. A **21**, S232–S240 (2003)
39. Wahl, K.J., Chromik, R.R., Lee, G.Y.: Quantitative in situ measurement of transfer film thickness by a Newton's rings method. Wear. doi: 10.1016/j.wear.2007.04.009
40. Johnson, K.L.: Contact mechanics. Cambridge University Press, Cambridge (1985)
41. Wahl, K.J., Singer, I.L.: Quantification of a lubricant transfer process that enhances the sliding life of a MoS_2 coating. Tribol. Lett. **1**, 59–66 (1995)
42. Bowden, F.P., Tabor, D.: The friction and lubrication of solids, part 2. Clarendon Press, Oxford (1964)
43. Uemura, M., Okada, K., Mogami, A., Okitsu, A.: Effect of friction mechanisms on friction coefficient of mos2 in an ultrahigh-vacuum. Lubric. Eng. **43**, 937–942 (1987)
44. Singer, I.L., Bolster, R.N., Wegand, J., Fayeulle, S., Stupp, B.C.: Hertzian stress contribution to low friction behavior of thin MoS_2 coatings. Appl. Phys. Lett. **57**, 995–997 (1990)
45. Briscoe, B.J., Evans, D.C.B.: The shear properties of langmuir-blodgett layers. Proc. Roy. Soc. Lon. Ser. A **380**, 389–407 (1982)
46. Heimberg J.A., Wahl K.J., Singer I.L., Erdemir A: Superlow friction behavior of diamond-like carbon coatings: time and speed effects. Appl. Phys. Lett. 78, 2449–2451 (2001)